

Research Article

Processing Window and Microstructure of NiCoCrAlY Coating Deposited on Cast Iron Using Multilayer Laser Cladding

Hao Liu ^{1,2}, Peijian Chen,³ Haifeng Yang,¹ Jingbin Hao,¹ Xianhua Tian,¹ Xiuli He,^{4,5} and Gang Yu^{4,5}

¹School of Mechanical and Electrical Engineering, China University of Mining and Technology, Xuzhou, China

²Jiangsu Key Laboratory of Mine Mechanical and Electrical Equipment, China University of Mining & Technology, Xuzhou, China

³School of Mechanics and Civil Engineering, China University of Mining and Technology, Xuzhou, Jiangsu, China

⁴Key Laboratory of Mechanics in Advanced Manufacturing, Institute of Mechanics, Chinese Academy of Sciences, Beijing, China

⁵School of Engineering Science, University of Chinese Academy of Sciences, Beijing 100049, China

Correspondence should be addressed to Hao Liu; liuhao56@cumt.edu.cn

Received 23 July 2018; Revised 21 November 2018; Accepted 31 December 2018; Published 17 February 2019

Academic Editor: Nikša Krstulović

Copyright © 2019 Hao Liu et al. This is an open access article distributed under the Creative Commons Attribution License, which permits unrestricted use, distribution, and reproduction in any medium, provided the original work is properly cited.

Cast iron is an iron-carbon alloy widely used in mechanical engineering. Nickel-base or cobalt-base alloy coatings prepared by laser cladding can improve the surface properties of cast iron, thereby increasing the service life of the components; however, due to the poor weldability and high carbon content of cast iron, the use of laser cladding to prepare alloy coatings faces many difficulties. To reduce the brittleness of the bonded interface, laser cladding was applied to the surface of cast iron using a multilayer deposition strategy. Through testing of the single-track laser cladding, the causes of defects in the coating are analysed, including poor bonding, slag inclusions, and pores. An analytical model based on mass and heat conservation is developed, and a processing window of laser tracks without defects is determined thereby. NiCoCrAlY alloy coating prepared by overlapping laser tracks mainly consists of γ -(Fe, Ni) dendrites and interdendritic M_7C_3 and $M_{23}C_6$ carbides. Although there are no cracks in a single laser track, cracks are detected when laser tracks are overlapped under the same process parameters. The increase in laser power helps to reduce cracking susceptibility on this occasion. The morphology of the grain in NiCoCrAlY alloy coating is mainly epitaxially grown columnar crystals. The increase in microhardness of the coating is mainly attributed to ductile dendrites, precipitated carbides, and grain refinement.

1. Introduction

Due to its excellent casting properties and cutting performance, cast iron is widely used in mechanical engineering and is particularly suitable for the manufacture of parts with complex shapes and cavities, such as machine tools, gear boxes, cylinder blocks, and cylinder heads. In some cases, compacted graphite cast iron, as a class of cast iron, can even replace carbon steel or alloy steel for the manufacture of high-strength, high-toughness parts, such as crankshafts, turbines, and worm gears; however, the surface properties of cast iron, including wear resistance and corrosion resistance, are not ideal [1]; therefore, the surface modification of cast

iron is a matter of great concern. Laser cladding is a promising surface modification technology. It uses high-power density laser beams to irradiate the substrate material and simultaneously adds cladding material so that the thin layer of the substrate surface and the cladding material are simultaneously melted, forming a melt pool. When the laser beam moves away, the melt pool solidifies, then a coating with the special properties of the cladding material is prepared on the substrate. The coating prepared by laser cladding has the advantages of a high bonding strength with the substrate, a compact microstructure, a small heat-affected zone, and little deformation of the workpiece. Preparing iron-based, nickel-based, cobalt-based alloy

coatings using laser cladding can effectively improve the service life of parts; however, laser cladding on cast iron surfaces faces unique difficulties. First of all, cracks are easily initiated from the side of coating/substrate interface due to the mismatch of the thermal expansion, or from the grain boundaries and pores inside the coating where the stresses are concentrated [2]. Cast iron generally contains strip-shape, sphere-shape, or vermicular-shape graphite. Xu et al. developed a macroscopic model of the laser cladding process and a microscopic model of graphite to explain the stress concentration at the graphite tip, which is the most likely source of a crack [3]. Yi et al. established a thermomechanical-coupled numerical model, showing that the stress concentration of the graphite tip during the laser cladding process is significantly affected by the shape and length of the graphite inclusion [4]. In the bonding zone, brittle acicular martensite and ledeburite are formed under rapid cooling conditions [5, 6], and graphite often is not completely melted [7]. These all result in degradation of the mechanical properties of the bonded area. When the stress at the graphite tip exceeds the yield strength, cracks develop and propagate. From this, it can be concluded that the concentrated stress and the brittle phase are the causes of cracking. Secondly, graphite in the matrix of cast iron is heated and gasified, resulting in pore formation in the coating [8], thus exerting an adverse effect on coating performance.

Preheating the cast iron before laser cladding is an effective way to solve these problems. Preheating reduces thermal stress [9], and eliminates graphite which acts as a crack source [10, 11]. Therefore, preheating reduces the crack sensitivity of cast iron. A common method of preheating is to put a workpiece into an electric furnace and heat the entire workpiece to a predetermined temperature. This method is inefficient, energy intensive, and is unsuitable for large workpieces that cannot fit in the furnace. As a result, local preheating has attracted the attention of some researchers. Huang and Zeng used an induction coil to preheat the front area of the laser scanning trace, thereby reducing the thermal stress within the workpiece, preventing crack initiation [12]; however, this method increases the complexity of the processing equipment. Lai et al. preheated the substrate directly using a laser beam and discovered that the formation of martensite could be avoided by increasing the scan length during preheating [13].

For the problems encountered during laser cladding of cast iron, a multilayer cladding strategy was proposed, which adopted reciprocating scanning with a low powder feed rate. The experimental results showed that depositing the first layer played a role of alloying the surface of the cast iron, as well as of local preheating. When subsequent layers were deposited, the resulting thermal cycles tempered the heat-affected zone. It was proved that this strategy could eliminate the hard brittle martensite and reduce the residual stress at the interface between the coating and the cast iron [14]. Furthermore, we mainly discuss the principal defects and their causes in multilayer laser cladding, and explore the processing window and microstructure of the NiCoCrAlY alloy coating on cast iron.

2. Material Design and Experimental Procedure

2.1. Material Design. The substrate material is compacted graphite cast iron (RuT300) and its microstructure consists of pearlite, ferrite, and graphite (Figure 1). Most of the graphite in the cast iron is vermicular, with a length of 10 μm to 200 μm , distributed between the metal matrix composed of pearlite and ferrite. The chemical composition of compacted graphite cast iron was as shown in Table 1. The substrate was cut into samples measuring 120 mm \times 60 mm \times 30 mm. Their surface was sanded and cleaned with acetone and absolute ethanol to remove the oxide layer before testing.

NiCoCrAlY powder, which is the first choice for metal bond coat in the preparing of double-layer thermal barrier coating [15], is selected as a cladding material. The chemical composition of the powder was as shown in Table 2. Ni, as the main element of the powder, has similar lattice constants to samples with γ -Fe in the cast iron. Ni and Fe can be infinitely mutually soluble and thus form a stable austenite at elevated temperatures. The elements of Cr and Co are expected to improve the wear resistance and corrosion resistance of the coating, respectively. The main purpose of adding a small amount of Al and Y components to the powder is to refine the grains. The NiCoCrAlY alloy is produced by gas atomization. The powder particles are mainly spherical or nearly spherical, with a particle size of 20 μm to 200 μm (Figure 2). Before testing, the alloy powder was dried using a high-temperature drying oven.

The main physical properties of the compacted graphite cast iron and cladding materials at room temperature are as shown in Table 3 [16, 17]. In addition to the thermal conductivity, the density, melting point, and thermal expansion coefficient of the cladding material and compacted graphite cast iron are similar, which is conducive to reducing the thermal stress between the coating and the substrate.

2.2. Experimental Design. A 1000 W Nd:YAG continuous laser with a laser wavelength of 1.064 μm was used in these experiments. A five-axis CNC table provided relative movement between the laser head and the substrate. The coaxial powder feed nozzle installed on the laser head is used to deliver the powder flow to the melt pool. The carrier gas was argon at a flow rate of 5 L/min. A multilayer scanning strategy was used to reduce brittleness and cracking sensitivity at the bonding interface [14]. The schematic diagram of laser cladding process is shown in Figure 3.

The experiments were carried out in two stages: in the first stage, single tracks were deposited with the purpose of exploring the processing window of multilayer laser cladding. The main processing parameters are laser power P , scanning speed V , and powder feed rate F . To study the influence of various parameters on the quality of the coating, a gradient method was used in the experimental design. In this method, one processing parameter continuously increases or decreases, whereas other process parameters are kept constant [2]. A laser spot (3-mm diameter) was used. The laser beam intensity is uniformly distributed in the cross

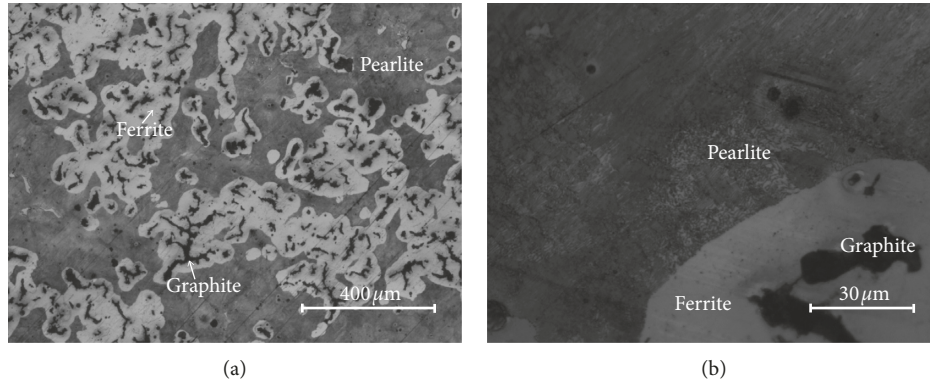


FIGURE 1: Microstructure of compacted graphite cast iron.

TABLE 1: CGI chemical elemental composition (mass fraction, wt.%).

Material	C	Si	Mn	P	S	Fe
CGI	3.6	2.7	0.2	<0.05	<0.02	Bal

TABLE 2: Chemical elemental composition of NiCoCrAlY alloy powder (mass fraction, wt.%).

Material	C	Ni	Co	Cr	Al	Y
NiCoCrAlY	0.5	Bal.	2.6	18.6	3.4	1.0

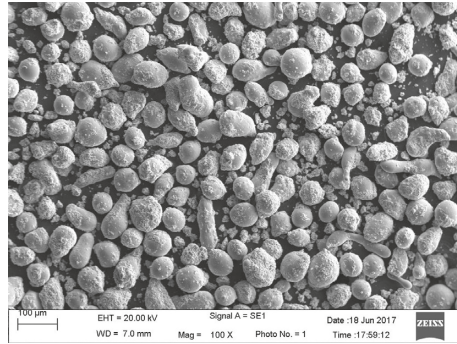


FIGURE 2: Morphology of NiCoCrAlY powder particle.

TABLE 3: Thermophysical properties of CGI and NiCoCrAlY.

Material	Density (kg/m ³)	Melting point (°C)	Thermal conductivity (W/m·K)	Heat capacity (J/kg·K)	Coefficient of linear thermal expansion (10 ⁻⁵ /K)
CGI	7090	1208	39	513	1.2*
NiCoCrAlY	7320	1330	4.3	501	1.4

*Data obtained at 18°C, and the remaining data arise from tests conducted at 20°C.

section perpendicular to the propagation direction. The powder flow transported by the coaxial nozzle converges to a Gaussian distribution on the substrate [18, 19]. Each laser track was deposited in six layers. The gradient technique was applied to reduce the number of cladding experiments [2]. The laser powers used in the experiments were as follows: 300 W, 400 W, 500 W, 600 W, and 700 W. The powder was

delivered at 1.67 g/min, 2.56 g/min, 3.45 g/min, and 4.33 g/min. The laser power and feed rate parameters were combined into three groups in terms of scanning speeds of 3 mm/s, 5 mm/s, and 7 mm/s. In this way, a total of 60 laser tracks were prepared. The cross section of each laser track was cut and observed using a stereoscopic microscope to detect the defects, including poor bonding, slag inclusions,

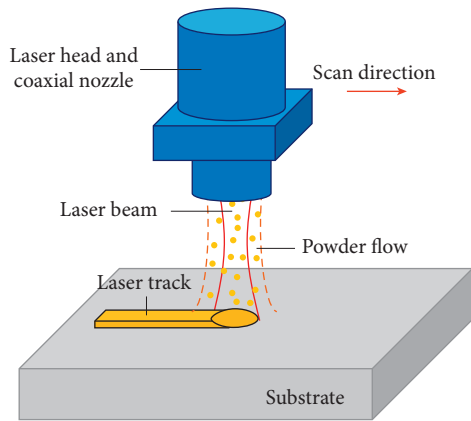


FIGURE 3: Schematic diagram of laser cladding process.

and pores. Based on the experimental results, the effect of process parameters on cladding quality was summarised, and the processing window for multilayer laser cladding was determined.

The purpose of the second stage of the experiment was to prepare the coating by overlapping the laser tracks using the optimised processing parameters. The coatings were cut along the cross-sectional direction, and polished, preparing the specimens for metallographic analysis. After etching with *aqua regia*, the microstructure and composition distribution of the cladding layer were analysed using a scanning electron microscope (SEM) (ZEISS EVO18 Special Edition) with an energy dispersive spectrometer (EDS). The phases were analysed (XRD) using a Rigaku Dmax-RB X-ray diffractometer using a Cu target with an operating voltage of 40 kV. An HXD-1000 microhardness tester was used to measure the hardness distribution from the coating to the substrate in the depth direction, and the load dwell time was 15 s using a fixed mass of 100 g.

3. Experimental Results

3.1. Surface Morphology and Defects. The main defects are the poor bonding with the substrate, slag inclusions, and pores in the coatings deposited by multilayer laser cladding. Figure 4 shows the surface morphology of laser tracks at a scanning velocity of 5 mm/s with various laser powers and powder feed rates. According to the results, the morphology of the laser tracks can be classified into discontinuous surface, critical surface, and continuous surface, which are represented by triangles, squares, and circles in Figure 4, respectively. The laser track with discontinuous surface is intermittent and consists of a row of unconnected spherical beads. The beads, with the diameter in the range of 2 mm to 3 mm, have very little bonding force and easily fall from the substrate. The critical surface is continuous, but with certain fluctuations in height. In addition, there are many slag inclusions seen on both sides of the laser tracks. Laser tracks with a continuous surface are relatively smooth, with few slag inclusions. When the powder feeding rate was kept constant, the surfaces of the laser tracks changed from discontinuous to critical, then continuous, as the laser power increased.

Slag inclusions often appear at side boundary of the laser tracks. The slag is granular, with a diameter of between 0.2 mm and 1 mm (much larger than the diameter of the powder particles). The number and diameter of slag inclusions increases with increasing powder feed rate. From the perspective of shape and location of slag inclusions, it could be inferred that an inclusion is formed by the solidification of many powder particles, which melt before reaching the substrate in the powder feeding processing. This agreed with the numerical simulation undertaken by Wen et al. [20]. The slag inclusions on the critical surface are the largest. As the laser power increases, the number of slag inclusions decreases. It could be inferred that this would induce defects, such as cracks, when overlapping the laser tracks to prepare a larger area of coating.

The cross sections of the laser tracks at different scanning speeds are shown in Figure 5. In the same group, the characteristics of the laser tracks show a clear trend: take a group of speeds of 5 mm/s as an example (Figures 4 and 5(b)), when the powder feed rate is 1.67 g/min, the laser track deposited at a laser power of 300 W is characterised by a discontinuous surface. It could be confirmed from Figure 5(b) that it does not metallurgically bond with the cast iron substrate. Increasing the laser power beyond 400 W, the laser track changes to a continuous surface and metallurgical bonding is achieved and pores are detected in the laser tracks. A large number of pores appear at the interface between the laser track and the substrate, and only a few appear inside the laser track. It can be seen that the pores are accompanied by poor bonding and could be eliminated with increasing laser power. The width of the laser tracks that reached a state of metallurgical bonding was about 3 mm, which is equivalent to the diameter of the laser spot.

When laser cladding is carried out at lower laser powers, and at a relatively large feed rate, the energy of the laser beam is almost fully absorbed by the powder flow, and the substrate would not receive enough energy to form a melt pool, leading to a discontinuous surface and a poor bond. On the other hand, if the laser power is too high and the feed rate is small, the melt pool would be excessively diluted, reducing the performance of the laser track. In addition, a smaller wetting angle, which is defined as the angle between the tangent of the contour of the laser track and the horizontal plane of the substrate surface, is required to ensure the quality of the laser track [21]. The wetting angle gradually increases as the feed rate increases. Comparing different groups of specimens, it can be seen that, as the scanning speed increases, the thickness of the laser track decreases to a significant extent. A too low scanning speed results in an excessive wetting angle; therefore, the preparation of a laser track of good quality requires a suitable combination of processing parameters (i.e., the processing window). This processing window is established based on the balance of mass and energy (Section 4.1).

3.2. Microstructure. According to the processing window, a dense, defect-free, metallurgically bonded laser track was obtained at a laser power of 900 W, a spot diameter of 2 mm,

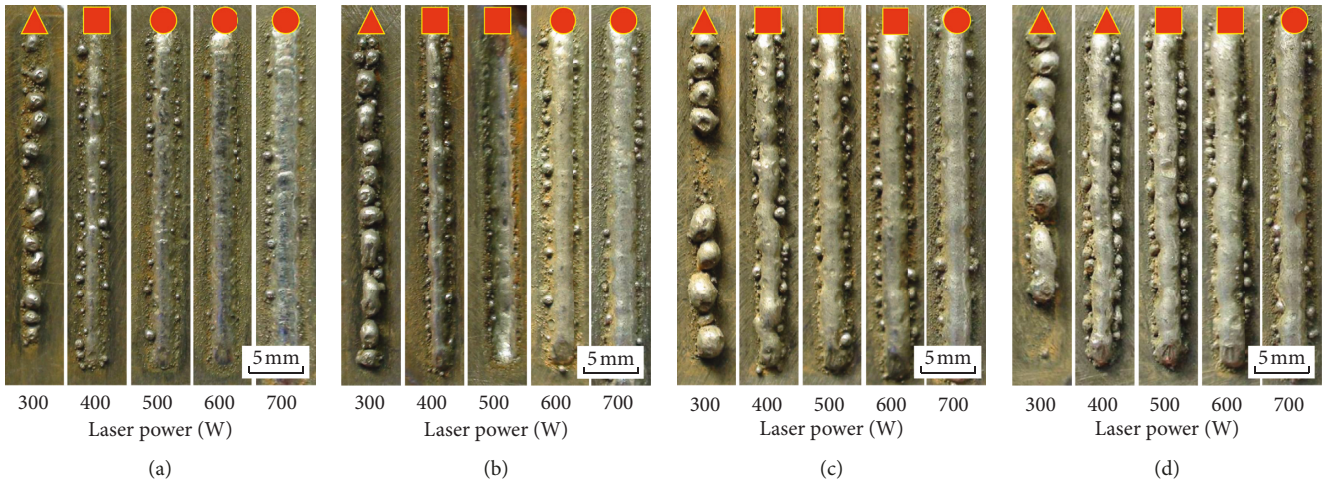


FIGURE 4: Surface morphology of laser tracks at the scanning velocity of 5 mm/s with various laser powers and powder feed rates of (a) 1.67 g/min, (b) 2.56 g/min, (c) 3.45 g/min, and (d) 4.33 g/min.

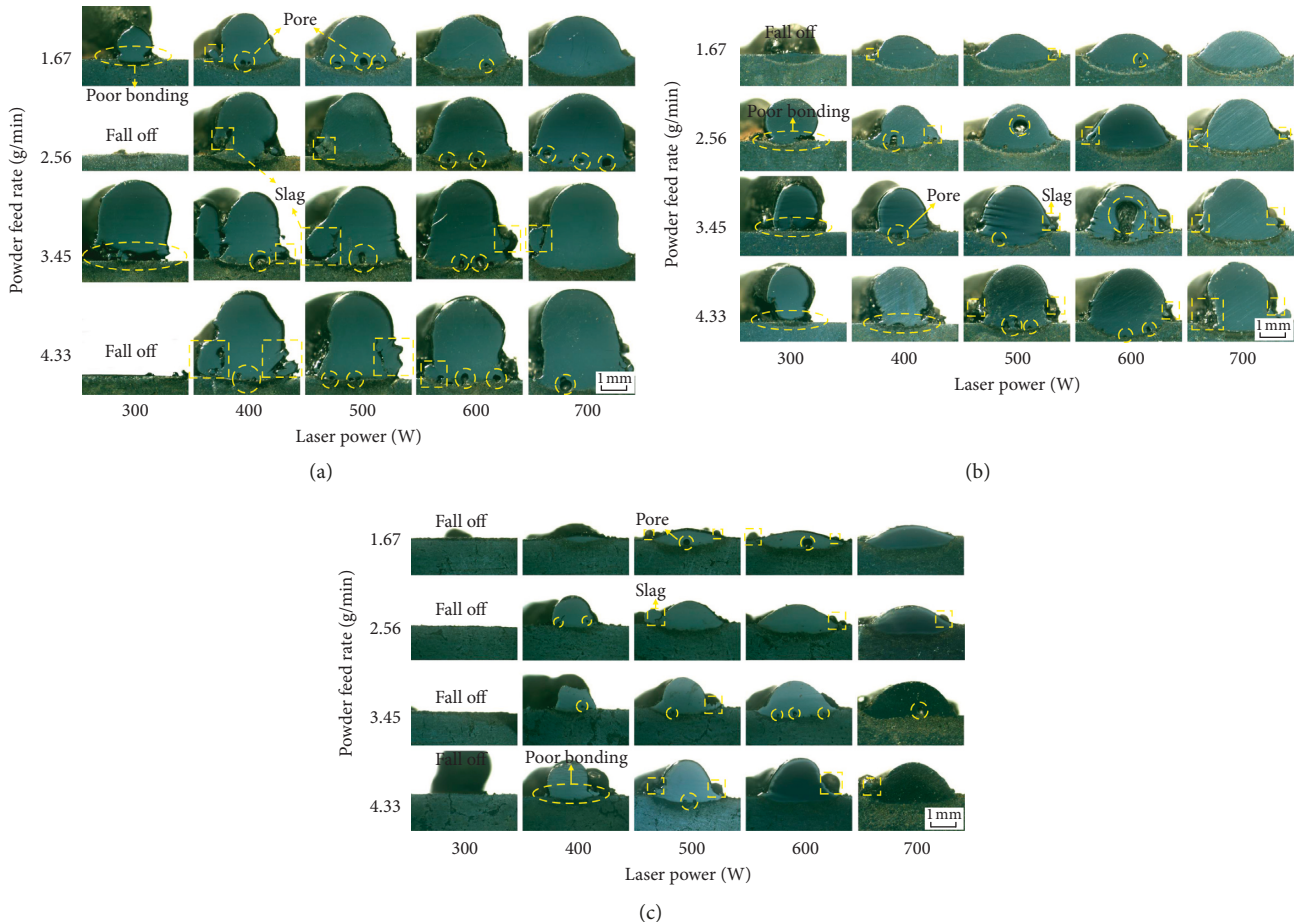


FIGURE 5: Cross section of laser tracks for laser cladding on compacted graphite cast iron at the scanning velocity of (a) 3 mm/s, (b) 5 mm/s, and (c) 7 mm/s.

a scanning speed of 6 mm/s, and a feed rate of 4.15 g/min. The scanning electron micrograph of the middle region in the cross section of the laser track is shown in Figure 6, and it can be seen that the microstructure is mainly composed of

grey dendrites and interdendritic precipitation phases. The average primary dendritic spacing is less than $10\ \mu\text{m}$ and the average secondary dendritic spacing is less than $1\ \mu\text{m}$, indicating that the grains were refined under rapid

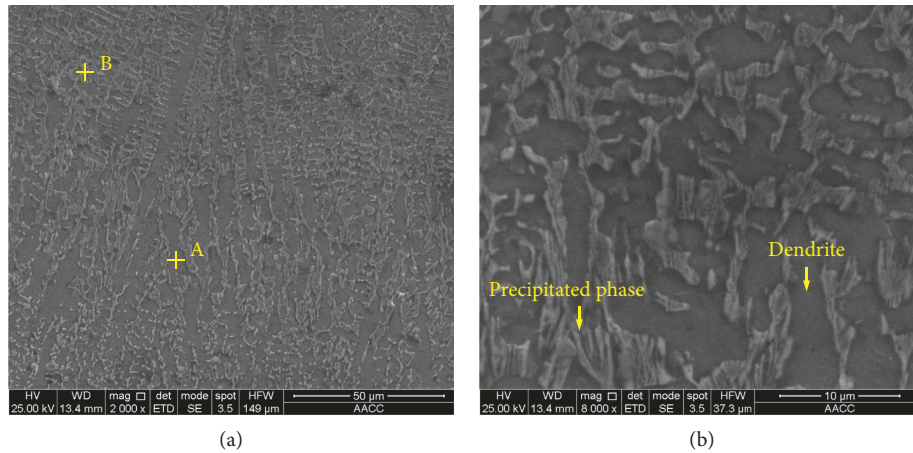


FIGURE 6: Cross-sectional SEM micrographs of NiCoCrAlY laser track. (a) 2000 \times image showing the location of EDS testing points and (b) 8000 \times image showing the dendritic structure.

solidification conditions imposed by the laser cladding process. The grey dendrites formed a continuous phase, and the interdendritic precipitates appeared as a framework. EDS analysis output is shown in Figure 7: the dendrites were rich in Fe and Ni, and the Cr content increased significantly in the interdendritic region.

The X-ray diffraction analysis output is shown in Figure 8. The NiCoCrAlY alloy coating is mainly composed of γ -(Fe, Ni) solid solution and M_7C_3 and $M_{23}C_6$ carbides, in which M represents Cr, Fe, or Ni. There may be other phases present in the microstructure, but in lower amounts and with weaker diffraction peaks. Combined with the results of EDS analysis, it could be inferred that the dendrite is the γ -(Fe, Ni) solid solution, in which Co and Al are dissolved. As a continuous phase, the refined γ -(Fe, Ni) solid solution dendrite provides ductility for the coating. The phases in the interdendritic region are carbides of M_7C_3 and $M_{23}C_6$ characterised by high hardness. Besides, there may be a small amount of low-melting point eutectic phase formed between the dendrites.

3.3. Microcracking. Coating covering the large areas of parts must be prepared by overlapping laser tracks. The high-temperature gradient caused by rapid solidification will generate thermal stresses in the deposited layer and substrate. The thermal stresses fluctuate and endure during the overlapping processing, readily resulting in cracking. To investigate the cracking, NiCoCrAlY coatings overlapped by eight laser tracks deposited with six layers were prepared on cast iron using different laser powers. The other process parameters used were as follows: laser spot diameter of 2 mm, scanning speed of 3 mm/s, powder feeding rate of 2.4 g/min, and an overlapping rate of 25%. The cross sections of coatings were cut, polished, etched, and examined under an optical microscope. Microcracks are found in the coating prepared using a laser power of 400 W (Figure 9). It can be seen that the microcracks originated from the equiaxed grains in the top of the coating and propagated along the grain boundary. The maximum width of the microcracks in

the coating reached 75 μm and the maximum length reached about 700 μm . The number and maximum width of cracks in the coatings are listed in Table 4. It can be seen that as the laser power increases, the number of cracks in the coatings decreases and the crack width decreases. No cracks are found in those coatings prepared using laser power outputs of more than 600 W. So, it could be concluded that high laser power suppresses the formation of microcracks.

The chemical component distributions along the depth direction of the coatings are compared in Figure 10. For the coating formed at a laser power of 400 W, the elements Fe and Ni, which come mainly from cast iron and alloy powder, respectively, are distributed in a stepwise fashion. Within about 580 μm from the top surface, the mass fraction of elemental Ni fluctuates around 60%, whereas the mass fraction of elemental Fe fluctuates around 20%. This zone corresponds to the last deposited layer with a depth of 602 μm (Table 4). At a distance of 580 μm to 600 μm , the mass fraction of elemental Ni decreases to 40%, whereas the mass fraction of elemental Fe increases to 40%. As the laser power increases, the distribution of elements along the depth direction gradually becomes uniform. At a laser power of 800 W, the distribution of Fe and Ni elements is relatively uniform, which reduces the tendency to cracking.

3.4. Epitaxial Growth. Figure 11 shows the optical micrograph of transverse section of the NiCoCrAlY coating. It can be seen from Figure 11(a) that the boundaries between individual layers are evident, revealing the pattern of layer-by-layer deposition. The predeposited material is remelted when depositing the subsequent layer; thus, the metallurgical bonding of each deposited layer is guaranteed. As is shown in Figure 11(b), with its high magnification, the microstructure at the bottom of the first deposited layer mainly consists of cell crystal and a small amount of undissolved graphite that comes from the molten substrate material. Figures 11(c) and 11(d) are magnified views showing the microstructure and boundaries of adjacent layers. It can be observed that the dominant morphology is

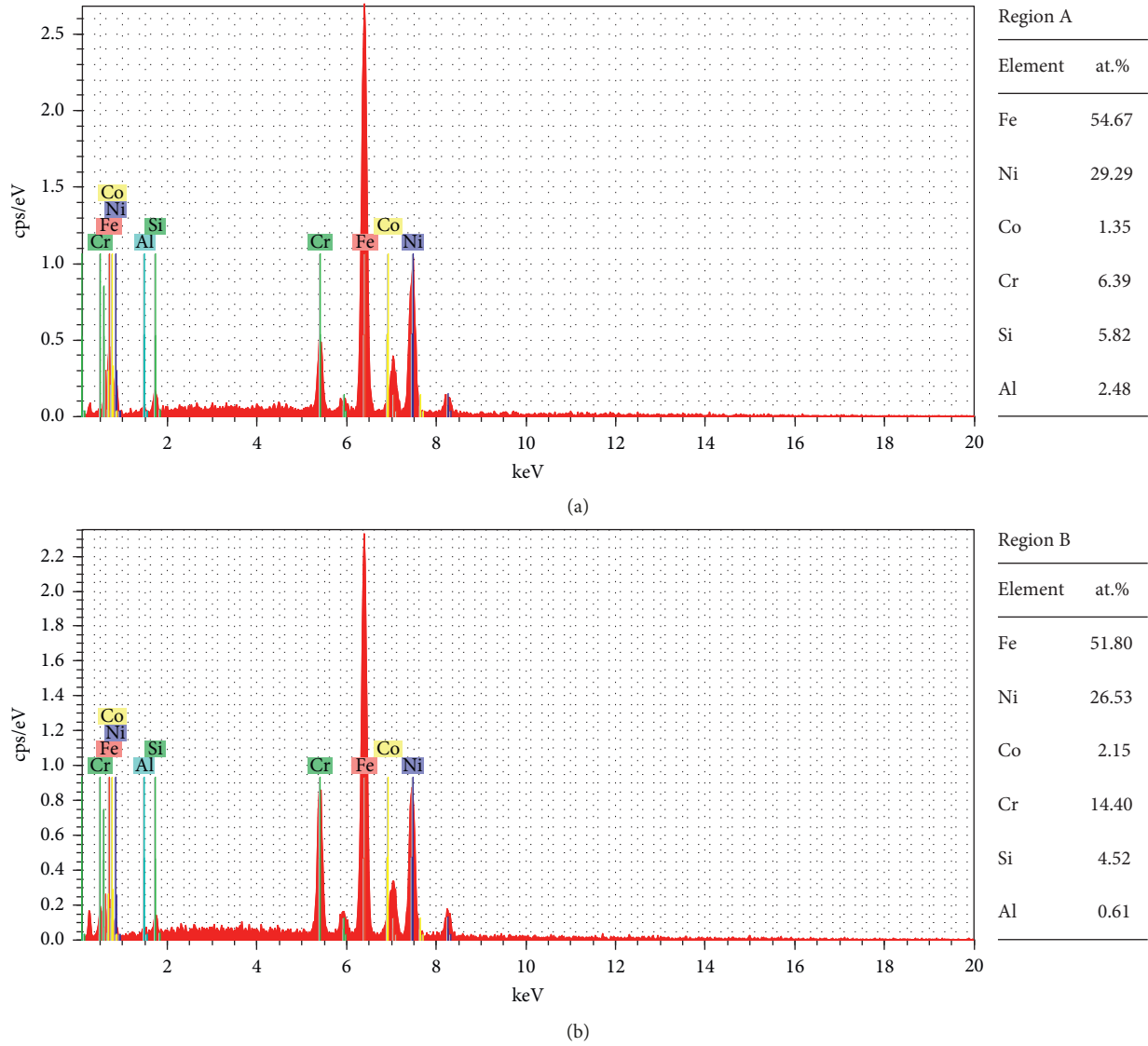


FIGURE 7: EDS results of dendritic and interdendritic region. (a) Region A and (b) region B.

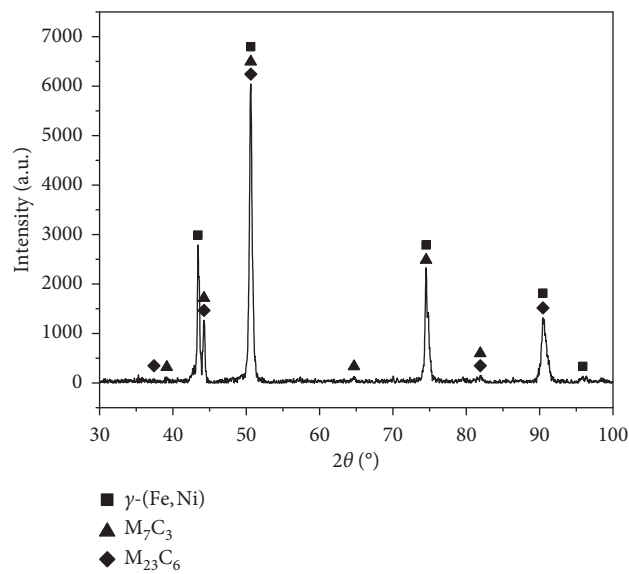


FIGURE 8: XRD pattern of NiCoCrAlY alloy coating.

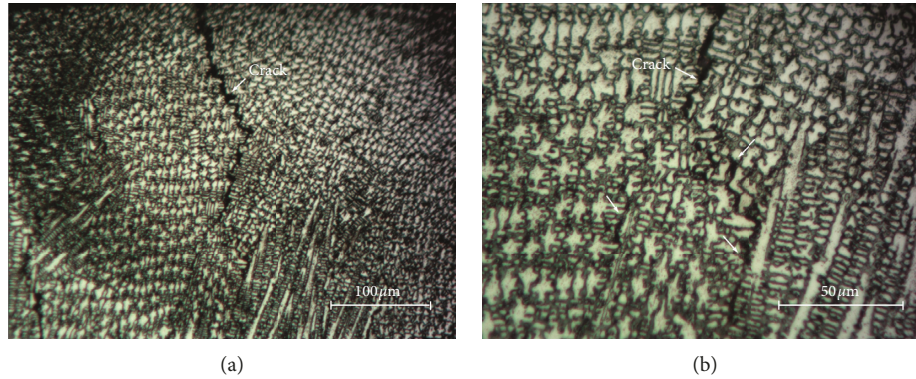


FIGURE 9: Microcracks in the coating prepared by overlapping laser tracks.

TABLE 4: State of microcracks in the coatings with different laser power outputs.

Laser power (W)	400	500	600	700	800
Number of microcracks	7	4	0	0	0
Maximum width of cracks (μm)	75	52	\	\	\
Thickness of the coating (μm)	828	1110	1583	1949	2420
Depth of the top layer (μm)	602	961	1006	1181	1454

aligned columnar dendrites in the centre of the coating. The direction of growth of the dendrites is nearly perpendicular to the substrate, which is opposite to that of the heat transfer flux. It should be pointed out that no planar grains are detected at the boundaries of each deposited layer. The crystallographic orientation and morphology of primary phase of subsequent layer are identical to those in the previous layer. These indicate that nucleation is avoided and the solidification of each subsequent layer begins by epitaxial growth. The morphology remains columnar in the middle of the last deposited layer in Figure 11(g), whereas the top of this layer is formed from equiaxed grains as seen in Figure 11(h). Therefore, the columnar-to-equiaxed transition (CET) is confirmed to have occurred during the solidification of the final layer. At the same time, it can be found that the dendrites of subsequent layers are much coarser than those of the previous layers. The mean primary dendrite arm spacing from the first layer to the fourth layer is $5.37 \mu\text{m}$, $5.66 \mu\text{m}$, $5.87 \mu\text{m}$, and $6.31 \mu\text{m}$, respectively. The refinement of grains is closely related to the cooling rate. The greater the cooling rate, the finer the crystal structure. The cooling rate of the subsequent layer decreases because of heat accumulation in the deposition processing, the dendrites then have more time to grow when the melt pool solidifies. These are the reasons why the dendrites formed in the subsequent layer are coarser.

In the middle of the coating, a columnar crystal structure with a direction perpendicular to the substrate is obtained by epitaxial growth among deposition layers. The ratio of the thickness of the columnar grain structure region to the total height of the coating (R_C) is defined to describe the proportion of columnar dendrites in the microstructure. With the increase in the number of deposited layers, the ratio gradually increases from 40.0% in the first layer to 63.9% in the sixth layer (Table 5).

3.5. Microhardness. Figure 12 shows the microhardness distributions ranging from the surfaces of coatings with different laser powers to the cast iron substrate. The bonding interfaces of each coating are aligned to allow comparison of the variations in microhardness in the coatings. The microhardness of NiCoCrAlY coating is between 350 HV and 500 HV, which is approximately two to three times the microhardness of the cast iron. According to Archard's theory, the increase in hardness increases the wear resistance of the surface. The coating prepared with a laser power of 400 W has an uneven microhardness distribution: its average microhardness is 376.4 HV. With increasing laser power, the microhardness distribution tends to become uniform and the average microhardness of the coating decreases. The heat-affected zone (HAZ) has the highest microhardness in each plot on Figure 12, a fact which could be attributed to the formation of martensite and bainite. It is worth noting that, with the increase of laser power, the maximum hardness measured in the HAZ is decreasing. From previous research [14], the depth of the HAZ is about 0.30 mm to 0.40 mm if the coating is deposited in a single layer; however, the depth of the high microhardness region for each coating in the HAZ is reduced to between 0.05 mm and 0.10 mm, because of the tempering effect induced by the thermal input of subsequent layer deposition.

4. Discussion

4.1. Causes of Defects. The formation of slag inclusions is related to the interaction of the laser beam and the powder flow (Figure 13). The laser beam below the coaxial nozzle has an hourglass shape, and the powder flow is convergent [18]. The powder particles are heated in flight and melt by absorbing laser energy before reaching the substrate. Simultaneously, the laser beam is attenuated by the powder particles before it irradiates the substrate. The relationship between the melt pool diameter (d_m) and the diameter of powder flow on the substrate (d_p) determines the conditions for formation of slag inclusions. When the melt pool diameter is less than the diameter of the powder flow, a portion of powder particles which are melt in the flight may fall from the edges of the melt pool or the unmolten surface of the substrate: these powder particles, in a molten state, merge to

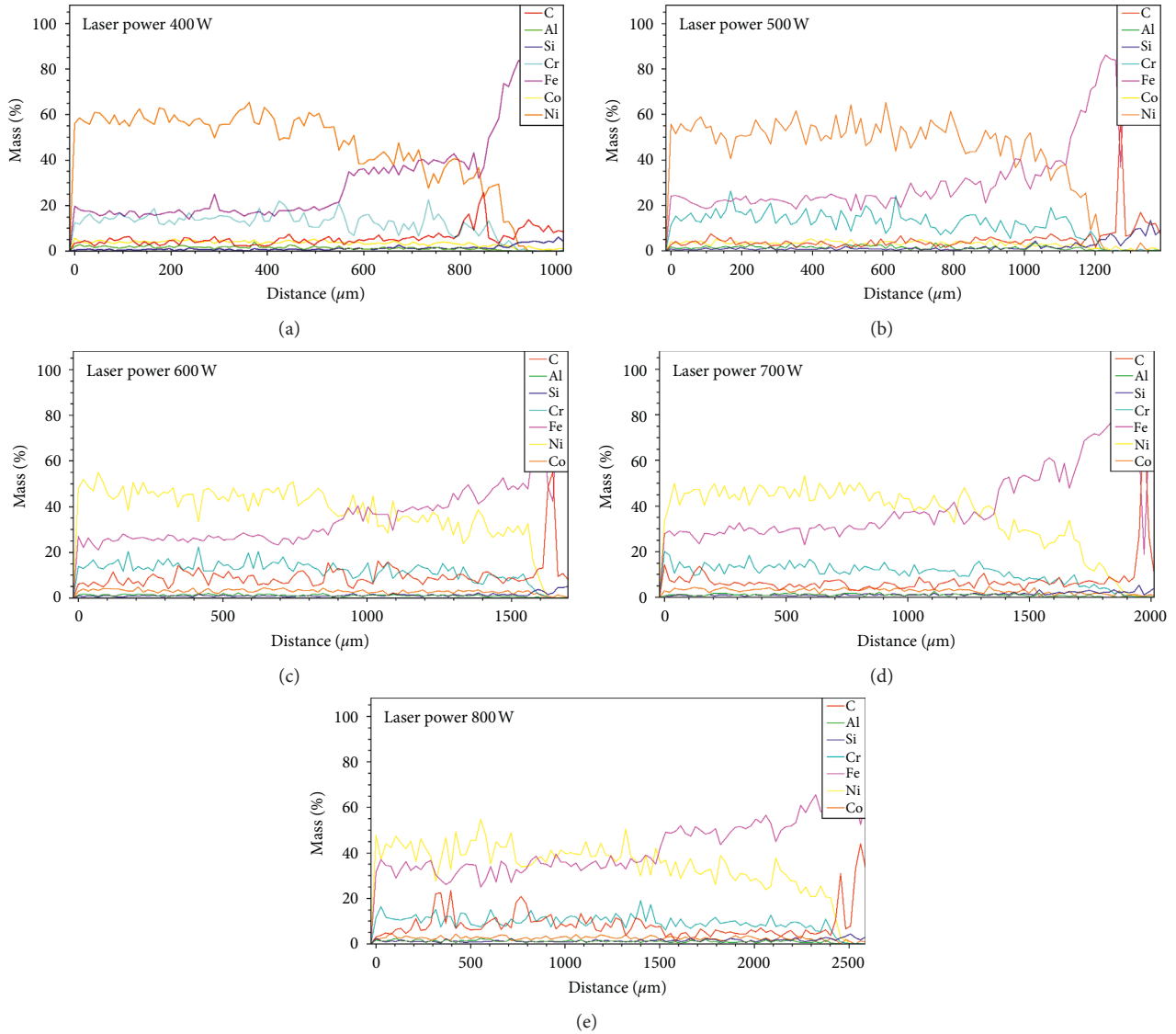
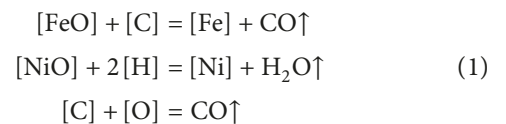


FIGURE 10: EDS line scanning analysis from coating to substrate: (a) 400 W, (b) 500 W, (c) 600 W, (d) 700 W, and (e) 800 W.

form melt beads. The beads which could not flow into the melt pool solidified and were transformed to slag inclusions. The increase of the powder feed rate causes more powder particles to melt, which is the reason why the size of the slag inclusions increases with increasing powder feed rate. When the melt pool diameter is greater than, or equal to, the diameter of powder flow, almost all of the powder particles delivered by the powder flow could fall into the melt pool, and solidify therewith. Thus, the formation of slag inclusions is avoided. The melt pool diameter increases with increasing laser power; therefore, the number of slag inclusions is decreased when the laser power is increased, which matched the experimental results. It could be inferred that the number of slag inclusions could be reduced by optimisation of the powder feeding process parameters or the rational design of the nozzle, which are both conducive to decreasing the diameter of the powder flow [19].

Combining Figures 4 and 5, it could be found that the surface state of the laser track reflects the quality of the laser cladding. When laser track has a continuous surface, it metallurgically bonds with cast iron substrate and has few pores. Otherwise, a laser track with a discontinuous, or critical, surface has a poor bond strength and many pores. It is found from Figure 5 that many pores appear at the interface between the coating and the substrate, and only a few appear within the coating. The formation of pores is related to the presence of gas that is insoluble in the melt pool. The gases are produced by metallurgical reactions in the melt pool:



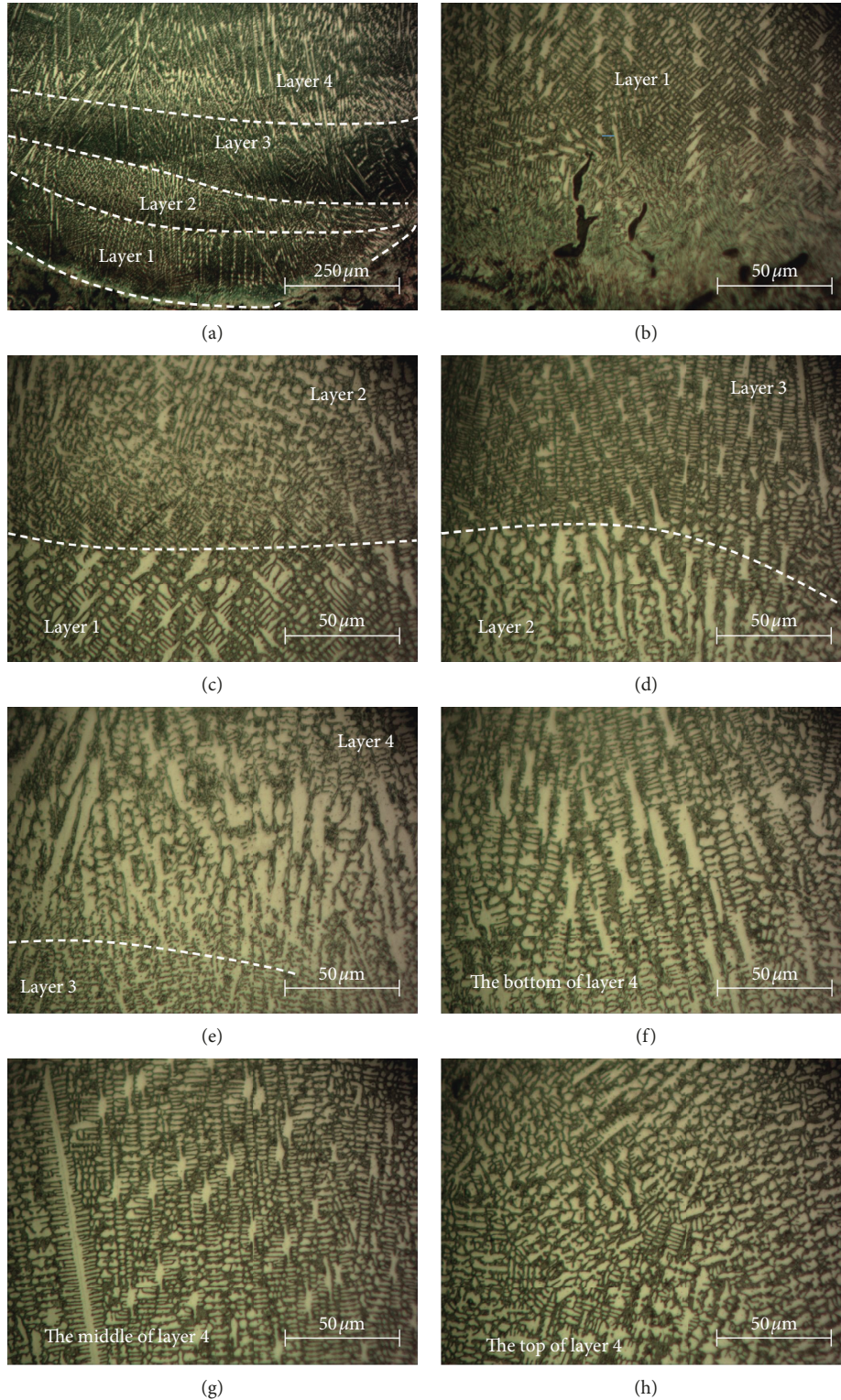


FIGURE 11: Microstructure of NiCoCrAlY coating at different locations.

If the convection is not strong, the metallurgical reactions mainly occur at the bottom of the melt pool, where the bubbles of reactant gases form. When the bubble's floating velocity (V_g) is less than the solidification velocity (V), the bubbles cannot escape in time during the

solidification of the melt pool, and then pores form. The floating velocity of bubbles could be expressed as

$$V_g = \frac{K(\rho_L - \rho_g)gr_g^2}{\mu}, \quad (2)$$

TABLE 5: Size of the columnar dendrite region and its variation with the number of deposited layers.

Layer number	1	2	3	4	5	6
Total height of coating (mm)	0.85	1.05	1.25	1.42	1.56	1.66
Thickness of columnar dendrite region (mm)	0.34	0.47	0.61	0.80	0.97	1.06
R_C (%)	40.0	44.8	48.8	56.3	62.2	63.9

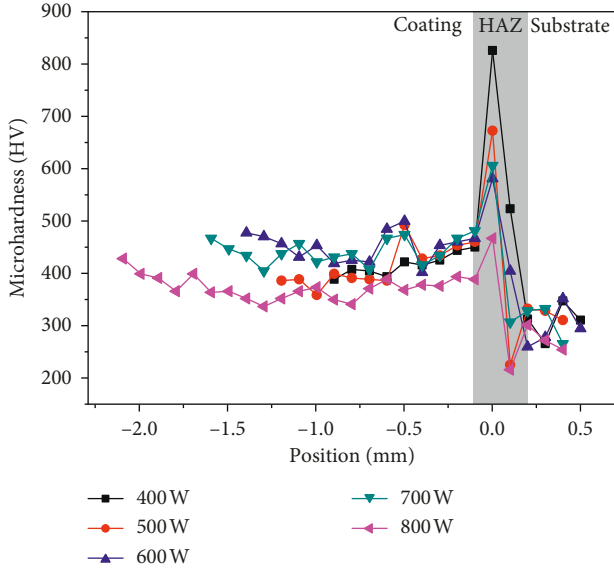


FIGURE 12: Microhardness distribution of coatings prepared under different laser output powers.

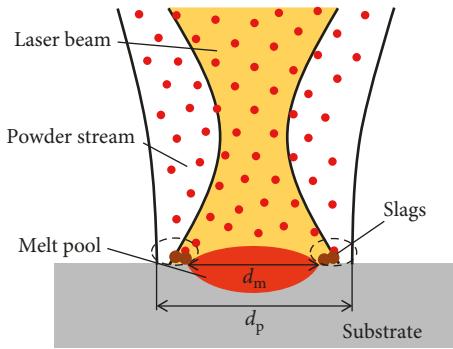


FIGURE 13: Schematic diagram of the formation of slag inclusions.

where K is the coefficient (taken here as $2/9$), ρ_L and ρ_g are the density of molten metal and gas density, respectively, r_g is the bubble radius, and μ is the viscosity of molten metal. Hence, the smaller the bubble's radius, the slower its floating velocity, and the easier the bubbles remain in the coating to form pores. Since the viscosity decreases with the increase of melt pool temperature, the pores could be prevented by increasing the melt pool temperature. This is confirmed by the fact that pores were not detected in the coating prepared under high laser power.

4.2. Processing Window. Figure 5 indicates that the metallurgical bonding between the substrate and the coating depends on the relationship between powder input and heat

input. The power density and interaction time are the two most important laser process parameters that directly affect the quality of laser track and are expressed as follows:

$$I = \frac{P}{\pi r_b^2}, \quad (3)$$

$$t_i = \frac{2r_b}{v}.$$

The minimum laser power density and power density required to ensure metallurgical bonding are defined as the critical laser power (P_c) and critical power density (I_c). The relationship between critical laser power and powder feed rate can be established by the balance of heat and mass:

$$I_c = \frac{P_c}{\pi r_b^2}. \quad (4)$$

Due to the laser material interaction mechanism, the laser energy is absorbed by a thin layer of metal surface. The substrate acts as the heat sink, for most of the heat is conducted downwards in the substrate. It is assumed that the laser irradiation is incident on the deposited layer with its thickness h ; thus, the temperature distribution along the depth direction can be approximated as [22]

$$T(z, t) = \frac{2A\epsilon I \sqrt{\alpha t}}{k} \text{ierfc}\left(\frac{z}{2\sqrt{\alpha t}}\right), \quad (5)$$

where z is the depth, t is the time, ϵ is the material emissivity, A is the energy absorption rate, I is the laser power density, α is the thermal diffusivity, k is the thermal conductivity, and ierfc is the integral of residual error function erfc , expressed as

$$\text{ierfc}(x) = \int_x^\infty \text{erfc}(x) dx. \quad (6)$$

Mass conservation in laser cladding can be expressed as

$$\eta F = \rho S v, \quad (7)$$

where η is the powder utilisation efficiency, ρ is the powder density, and S is the cross-sectional area of the laser track. It can be seen from the experimental results that when the critical metallurgical bonding state is reached, the width of the laser track is close to the laser beam diameter. The height of the laser track, with its single layer, is much less than the width of the laser track; thus, the cross-sectional area of the deposited layer can be approximately expressed as

$$S = h r_b, \quad (8)$$

where h is the height of the laser track. Combining equations (8) and (7), the height of the deposited layer can be expressed as

$$h = \frac{\eta F}{\rho v r_b} \quad (9)$$

The temperature at the bottom of the deposited layer should reach the melting point so that metallurgical bonding can be achieved; thus,

$$T(h, t_i) = T_m \quad (10)$$

From equations (4)–(10), the critical power density could be expressed as

$$I_c = \frac{kT_m}{2A\varepsilon\sqrt{\alpha t_i}} \left[\operatorname{ierfc} \left(\frac{\eta F}{2\rho v r_b \sqrt{\alpha t_i}} \right) \right]^{-1} \quad (11)$$

Substituting material parameters of powder into equation (11), the relationship between the critical power density and the powder feed rate can be obtained. The interaction times t_i used in the experiments were 0.43 s, 0.60 s, and 1.00 s, respectively. Each set of experiments corresponds to a critical curve (Figure 14). The calculated critical powers matched the experimental results and, as can be seen from Figure 14, the critical laser power density increases as the powder feed rate increases. At the same powder feed rate, the shorter the interaction time, the higher the critical laser power density. This tendency is also consistent with that observed experimentally.

The curves in Figure 14 could be to define a processing window to guide the selection of processing parameters in laser cladding. Each point in this window, calling a processing point, represents a combination of process parameters, including laser power, laser spot diameter, powder feed rate, and scan speed. When using a combination of process parameters located below the critical laser power density curve, the laser track cannot be metallurgically bonded to the substrate. When the processing point is on the critical power density curve, although the laser track can be metallurgically bonded to the substrate, it often has many pores and a critical surface with slag defects is formed. A well-bonded laser track, free from defects, could be obtained using processing points above the corresponding curve. It was worth noting that too high a power density increases the dilution, reducing the performance of the coating process [23], although the increase in laser power density can play a role in preventing pores and slag inclusions.

4.3. Cracking Analysis. Cracking is closely related to the stress state in the coating. When the melt pool solidifies, its shrinkage is limited by the surrounding metal, resulting in tensile stress and tensile plastic deformation. The region in the vicinity of the melt pool is subjected to the tensile stress in the heating period, and then is subjected to tensile stress in the cooling period. The microcracks appearing inside the coating are solidification cracks; that is, hot cracking occurred. In the solidification phase, γ -(Fe, Ni) dendrites precipitate first, a large number of dendrite nucleates and grows, and liquids with large solute contents and impurities are enclosed in the gaps between the dendrites to form a liquid film. In the late stage of solidification, the liquid

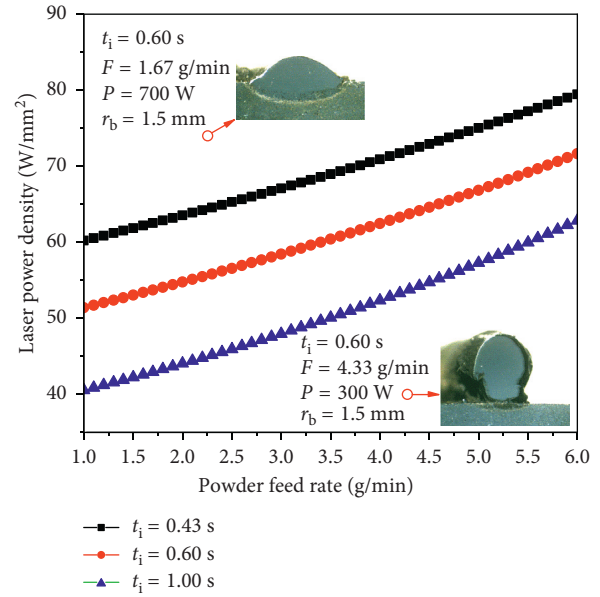


FIGURE 14: Processing window for laser cladding of Ni-based alloy powder on cast iron substrate in an I vs. F representation.

shrinks, resulting in microscopic holes forming in the grain boundary due to lack of solidification feeding caused by the sealing. Under the action of tensile stress, the liquid film and holes are pulled apart, thereby causing microcracking. These microcracks propagate along the grain boundaries under the effect of a repetitive thermal stress induced by the overlapping of laser tracks.

It is found, in the experiments, that cracking is suppressed by increasing the laser power output. Insufficient laser energy input leads to the uneven distribution of elements in the depth direction, and, in particular, a significant change in Fe and Ni contents at remelting boundaries (Figure 10(a)). This results in local thermal stress due to the mismatch of physical properties; however, the convection of the melt pool, as driven by surface tension, gravity, and buoyancy, tends to become stronger with increasing laser power. Meanwhile, the enlarged melt pool remelts more deposited material when overlapping the laser track. Thus, the composition and microstructure are much more uniform. Additionally, the temperature gradient from the coating to the HAZ decreases because the whole temperature of the superficial zone of substrate rises with higher power laser irradiation. These all decrease the thermal stress and reduce the cracking sensitivity as a result.

4.4. Conditions for Epitaxial Growth. It has been demonstrated that directionally solidified components with columnar grain structure are superior to equiaxed parts in terms of high-temperature strength, creep resistance, and thermal fatigue properties, due to the absence of a grain boundary normal to the principal axis of stress [24]. Thus, the coating with aligned columnar dendrites is expected, on the compacted cast iron substrate, to result in excellent performance. This aim could be achieved by layer-to-layer epitaxial growth in the multilayer laser cladding method

(Figure 11). In this way, the columnar dendrites of the previous layer are reproduced in the subsequent deposited layer.

The CET (columnar to equiaxed transition) was observed in single-layer deposition with various combinations of process parameters. At a given composition, the microstructural morphology of the clad metal depends on the local solidification conditions such as solidification rate V and temperature gradient G at the solid/liquid interface of the melt pool. The relationships between the local solidification conditions and grain morphology were established by Gaumann et al. as [25]:

$$\frac{G^n}{V} = a \left[\sqrt[3]{\frac{-4\pi N_0}{3 \ln(1-\phi)} \cdot \frac{1}{n+1}} \right]^n, \quad (12)$$

where a and n are material-dependent constants, N_0 is the number of nucleation sites, and ϕ is the volume fraction of equiaxed grains. As N_0 is a constant parameter for the selected material, and ϕ depends on G^n/V , therefore, G^n/V is considered as a control parameter governing the microstructure of the morphology of the coating. The microstructure selection map obtained by Gaumann et al. is shown in Figure 15 [25].

G^n/V can decrease by several orders of magnitudes from the bottom to top of melt pool induced by the laser beam, as evinced by experimental results [26]. Therefore, the solidified morphological variation from columnar dendrites to equiaxed grains at the top of each deposited layer is almost inevitable. To obtain epitaxial growth of columnar dendrites, a sufficient remelting of equiaxed grains of previous layer must be achieved when the subsequent layer is deposited (Figure 16), as expressed by

$$h_{r,i+1} \geq h_{e,i}, \quad (13)$$

where i represents the number of clad layers, h_r represents the remelting depth, and h_e represents the depth of the equiaxed crystal region.

Expecting certain geometric conditions, the chemical composition, and phase are also key factors governing epitaxial growth: if the composition of the clad alloy is the same as that of the substrate, epitaxial growth occurs during solidification; however, when the clad material has a different composition to that of the substrate, epitaxial growth occurs only if the first phase to solidify is the γ -phase, according to the findings arising from trial deposition of MCrAlY alloys onto an SX Ni-based superalloy by laser cladding [27]. When NiCoCrAlY alloy is deposited onto the compacted cast iron using a multilayer method, as mentioned above, the primary phase in the solidified alloy is γ -(Fe, Ni) and the compositions of adjacent layers are getting closer as the process proceeds. Depositing the subsequent layer only remelts the top of the previous solidified alloy layer. The substrate of cast iron no longer melts after depositing the first layer. Thus, each subsequent layer is solidified from its previous layer that has a similar composition, instead of the cast iron substrate. Consequently, the conditions of primary phase and composition for epitaxial growth are satisfied naturally between layers in multilayer laser cladding.

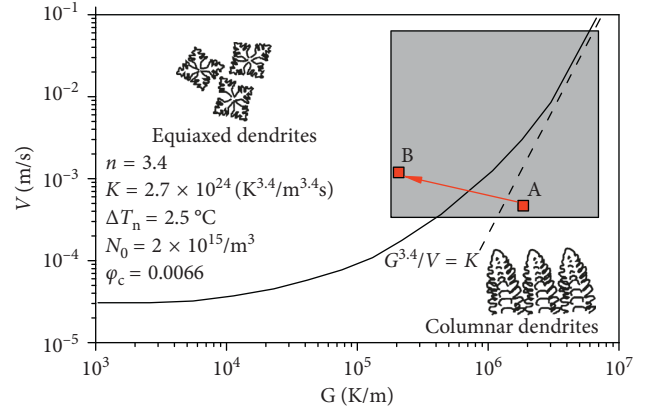


FIGURE 15: Microstructure selection map showing the expected solidification morphology as a function of G and V . The red arrow line shows the variation of conditions from the bottom of the melt pool (point A) to the top (point B), which is typical for the laser cladding. The parameter values were from the experimental results [26].

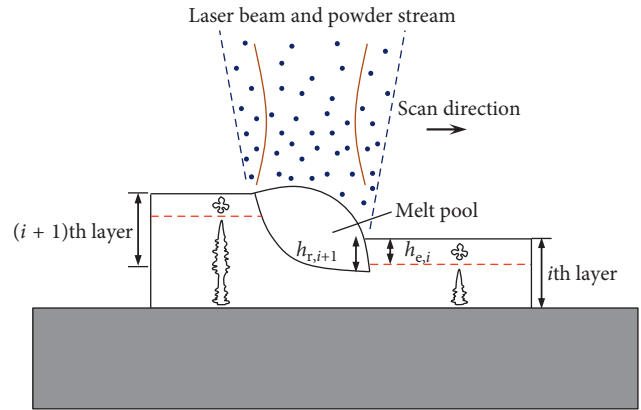


FIGURE 16: Epitaxial growth in multilayer laser cladding.

4.5. Microhardness Analysis. The increase in the microhardness of the NiCoCrAlY coatings is attributed to ductile dendrites, precipitated carbides, and grain refinement. The dendrites of γ -(Fe, Ni) exhibit good toughness. With sufficient Al and Co dissolved therein, lattices of this solid solution are distorted. The dislocation glide requires additional energy to cross the distorted lattices during microscale deformation; thus the strength and hardness of the material are improved. The carbides M_7C_3 and $M_{23}C_6$ are characterised by high hardness, act as strengthening phases, and are uniformly dispersed in the interdendritic region. The micronano carbides also play a role of hindering dislocation gliding. This microstructural feature is a well-known method to improve the mechanical properties of a material, called dispersion strengthening. Due to the high cooling rate, the dendritic grains in the coating do not have sufficient time to grow, so the grain size is much smaller than that of the as-cast alloy. According to the Hall-Petch equation, the strength increases with the decrease of grain size. Consequently, the refinement of dendrite grains contributes to the increase in microhardness.

It is found that the average microhardness decreases with the increase in laser output power. The main reason for this is the decrease in volume fraction of carbides seen in coatings prepared at higher laser power outputs. The reduction of the maximum hardness in the HAZ is attributed to the effect of heat accumulation in the substrate, which leads to a decrease in the cooling rate, resulting in a reduced volume fraction of hard martensite in the HAZ [14]. Comparing Figures 10 and 11, it can be seen that the uniformity of the microhardness distribution along the depth direction within the coating is related to the distribution of the chemical components therein. A more uniform microhardness distribution is obtained under fully developed Marangoni convection in the melt pool as induced by a higher laser power output [28].

5. Conclusion

To reduce the brittleness of the bonding interface, NiCoCrAlY alloy coatings on cast iron were prepared by multilayer laser cladding. Tests were conducted on single laser tracks. Defects in the laser tracks mainly include slag inclusions, pores, and poor bonding to the substrate. The formation of slag inclusions is related to the interaction between the laser beam and the powder flow. The appearance of pores is related to those gases present that are insoluble in the melt pool. These gases are produced by metallurgical chemical reactions. To ensure metallurgical bonding between the coating and the substrate and to suppress the generation of slag inclusions and pores, sufficient laser power must be applied. An analytical model based on mass and heat conservation is developed to calculate the critical laser power (P_c). The processing window of laser tracks without defects is determined by this model; however, cracks may still occur when overlapping the laser tracks. Such cracking is mainly attributed to thermal stress and nonuniform component distribution. It is confirmed that the cracking is eliminated by increasing the applied laser power output. The columnar dendrites occupied the centre of the coating by epitaxial growth of each deposited layer. The microhardness of the NiCoCrAlY coating is two to three times that of the cast iron substrate. The increase in microhardness is mainly due to ductile dendrites, precipitated carbides, and grain refinement.

Nomenclature

a :	Material-dependent constant
A :	Energy absorption rate (%)
d_m :	Melt pool diameter (mm)
d_p :	Powder flow diameter (mm)
F :	Powder feeding rate (kg/s)
G :	Temperature gradient (K/mm)
h :	Height from the surface (mm)
h_e :	Depth of the equiaxed crystal region (mm)
h_r :	Remelting depth (mm)
I :	Laser power density (W/mm^2)
I_c :	Critical power density (W/mm^2)
k :	Thermal conductivity ($W/(m\cdot K)$)

K :	Coefficient for bubbles velocity
n :	Material-dependent constant
N_0 :	Number of nucleation sites (mm^{-3})
P :	Laser power (W)
P_c :	Critical laser power (W)
r_b :	Laser beam radius (mm)
r_g :	Bubble radius (mm)
S :	Cross-sectional area (mm^2)
t :	Time (s)
t_i :	Interaction time (s)
T :	Temperature (K)
T_m :	Melting temperature (K)
v :	Laser scanning velocity (mm/s)
V :	Solidification velocity (mm/s)
Z :	Depth (mm)
α :	Thermal diffusivity (mm^2/s)
ε :	Material emissivity
η :	Utilisation ratio of powder
μ :	Viscosity of molten metal ($kg/(m\cdot s)$)
ρ :	Density (kg/mm^3)
φ :	Volume fraction of equiaxed grains.

Data Availability

The data used to support the findings of this study are available from the corresponding author upon request.

Conflicts of Interest

The authors declare that they have no conflicts of interest.

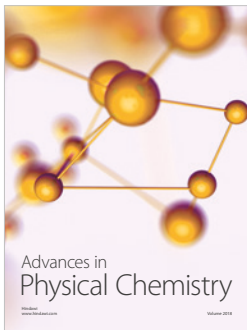
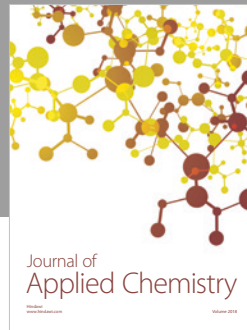
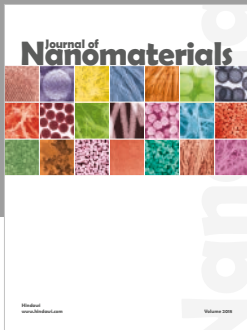
Acknowledgments

The authors acknowledge the Natural Science Foundation of Jiangsu Province (Grant no. BK20160258), the China Postdoctoral Science Foundation (Grant no. 2015M581881), and a project funded by the Priority Academic Program Development of Jiangsu Higher Education Institutions (PAPD).

References

- [1] B. Podgornik, J. Vizintin, I. Thorbjornsson et al., "Improvement of ductile iron wear resistance through local surface reinforcement," *Wear*, vol. 274-275, pp. 267-273, 2012.
- [2] V. Ocelík, U. de Oliveira, M. de Boer, and J. T. M. de Hosson, "Thick Co-based coating on cast iron by side laser cladding: analysis of processing conditions and coating properties," *Surface and Coatings Technology*, vol. 201, no. 12, pp. 5875-5883, 2007.
- [3] P. Y. Xu, Y. C. Liu, P. Yi, C. F. Fan, and C. K. Li, "Research on variation and stress status of graphite in laser cladding process of grey cast iron," *Materials Science and Technology*, vol. 30, no. 14, pp. 1728-1734, 2013.
- [4] P. Yi, Y. Liu, C. Fan, X. Zhan, P. Xu, and T. Liu, "Impact analysis of the thermal mechanical coupling characteristics of graphite morphologies during laser cladding of gray cast iron," *Optics and Laser Technology*, vol. 90, pp. 52-64, 2017.
- [5] H. Yan, A. Wang, Z. Xiong, K. Xu, and Z. Huang, "Microstructure and wear resistance of composite layers on a ductile

- iron with multcarbide by laser surface alloying,” *Applied Surface Science*, vol. 256, no. 23, pp. 7001–7009, 2010.
- [6] R. Arabi Jeshvaghani, M. Jaberzadeh, H. Zohdi, and M. Shamanian, “Microstructural study and wear behavior of ductile iron surface alloyed by Inconel 617,” *Materials and Design (1980-2015)*, vol. 54, pp. 491–497, 2014.
- [7] Y. Liu, X. Zhan, P. Yi, T. Liu, B. Liu, and Q. Wu, “Research on the transformation mechanism of graphite phase and microstructure in the heated region of gray cast iron by laser cladding,” *Optics and Laser Technology*, vol. 100, pp. 79–86, 2018.
- [8] S. X. Yan, S. Y. Dong, B. S. Xu, Y. J. Wang, W. B. Ren, and J. X. Fang, “Carbon diffusions in the NiCuFeBSi alloy layer treated by laser cladding on grey cast iron,” *Rare Metal Materials and Engineering*, vol. 43, pp. 2182–2186, 2014.
- [9] R. Jendrzejewski, G. Śliwiński, M. Krawczuk, and W. Ostachowicz, “Temperature and stress during laser cladding of double-layer coatings,” *Surface and Coatings Technology*, vol. 201, no. 6, pp. 3328–3334, 2006.
- [10] Z. Lestan, M. Milfelner, J. Balic, M. Brezocnik, and I. Karabegovic, “Laser deposition of Metco 15E, Colmony 88 and VIM CRU 20 powders on cast iron and low carbon steel,” *The International Journal of Advanced Manufacturing Technology*, vol. 66, no. 9–12, pp. 2023–2028, 2012.
- [11] C.-M. Lin, A. S. Chandra, L. Morales-Rivas et al., “Repair welding of ductile cast iron by laser cladding process: microstructure and mechanical properties,” *International Journal of Cast Metals Research*, vol. 27, no. 6, pp. 378–383, 2014.
- [12] Y. Huang and X. Zeng, “Investigation on cracking behavior of Ni-based coating by laser-induction hybrid cladding,” *Applied Surface Science*, vol. 256, no. 20, pp. 5985–5992, 2010.
- [13] Q. Lai, R. Abrahams, W. Yan et al., “Effects of preheating and carbon dilution on material characteristics of laser-cladded hypereutectoid rail steels,” *Materials Science and Engineering: A*, vol. 712, pp. 548–563, 2018.
- [14] H. Liu, J. Hao, Z. Han, G. Yu, X. He, and H. Yang, “Microstructural evolution and bonding characteristic in multi-layer laser cladding of NiCoCr alloy on compacted graphite cast iron,” *Journal of Materials Processing Technology*, vol. 232, pp. 153–164, 2016.
- [15] S. Uwe, L. Christoph, and F. Klaus, “Some recent trends in research and technology of advanced thermal barrier coatings,” *Aerosol Science and Technology*, vol. 7, pp. 73–80, 2003.
- [16] X. C. Zhang, B. S. Xu, H. D. Wang, and Y. X. Wu, “Modeling of the residual stresses in plasma-spraying functionally graded ZrO₂/NiCoCrAlY coatings using finite element method,” *Materials and Design*, vol. 27, pp. 308–315, 2006.
- [17] K. A. Khor and Y. W. Gu, “Effects of residual stress on the performance of plasma sprayed functionally graded ZrO₂/NiCoCrAlY coatings,” *Materials Science and Engineering: A*, vol. 277, no. 1-2, pp. 64–76, 2000.
- [18] H. Liu, X. L. He, G. Yu et al., “Numerical simulation of powder transport behavior in laser cladding with coaxial powder feeding,” *Science China Physics, Mechanics and Astronomy*, vol. 58, p. 104701, 2015.
- [19] H. Liu, J. Hao, G. Yu et al., “A numerical study on metallic powder flow in coaxial laser cladding,” *Journal of Applied Fluid Mechanics*, vol. 9, no. 7, pp. 2247–2256, 2016.
- [20] S. Y. Wen, Y. C. Shin, J. Y. Murthy, and P. E. Sojka, “Modeling of coaxial powder flow for the laser direct deposition process,” *International Journal of Heat and Mass Transfer*, vol. 52, no. 25-26, pp. 5867–5877, 2009.
- [21] T. E. Abioye, D. G. McCartney, and A. T. Clare, “Laser cladding of Inconel 625 wire for corrosion protection,” *Journal of Materials Processing Technology*, vol. 217, pp. 232–240, 2015.
- [22] W. W. Duley, *CO₂ Laser Effects and Applications*, Academic Press, New York, NY, USA, 1976.
- [23] H. Liu, G. Yu, X. L. He, H. F. Yang, and Z. T. Han, “Microstructural and mechanical properties of a NiCoCrAlY coating prepared by laser cladding on a compacted graphite cast iron surface,” *Lasers in Engineering*, vol. 37, pp. 273–289, 2017.
- [24] M. Gäumann, S. Henry, F. Cléton, J.-D. Wagnière, and W. Kurz, “Epitaxial laser metal forming: analysis of microstructure formation,” *Materials Science and Engineering: A*, vol. 271, pp. 232–241, 1999.
- [25] M. Gäumann, C. Bezençon, P. Canalis, and W. Kurz, “Single-crystal laser deposition of superalloys: processing-microstructure maps,” *Acta Materialia*, vol. 49, pp. 1051–1062, 2001.
- [26] L. Wang, S. D. Felicelli, and J. E. Craig, “Experimental and numerical study of the LENS rapid fabrication process,” *Journal of Manufacturing Science and Engineering*, vol. 131, p. 041019, 2009.
- [27] C. Bezençon, A. Schnell, and W. Kurz, “Epitaxial deposition of MCrAlY coatings on a Ni-base superalloy by laser cladding,” *Scripta Materialia*, vol. 49, pp. 705–709, 2003.
- [28] Z. Gan, H. Liu, S. Li, X. He, and G. Yu, “Modeling of thermal behavior and mass transport in multi-layer laser additive manufacturing of Ni-based alloy on cast iron,” *International Journal of Heat and Mass Transfer*, vol. 111, pp. 709–722, 2017.



Hindawi

Submit your manuscripts at
www.hindawi.com

